PROCEEDINGS, 50th Workshop on Geothermal Reservoir Engineering
Stanford University, Stanford, California, February 10-12, 2025
SGP-TR-229

Mixed-Dimensional Approach for Compositional Multiphase Flow in High-Enthalpy Fractured Geothermal Reservoirs

Omar Duran[1,2], Veljko Lipovac[1] and Inga Berre[1]

[1]University of Bergen, Bergen, Norway

[2]omar.duran@uib.no

Keywords: mixed-dimensional compositional flow model, fractured media, non-isothermal flow, high-enthalpy geothermal simulation

ABSTRACT

We present a novel multiphase compositional model for geothermal reservoir simulation that incorporates phase separation phenomena and explicitly represents fractures. Mass and heat transfer in porous media typically use temperature as an independent variable, but this requires procedures for variable substitution during phase transitions. In contrast, the overall composition formulation avoids such substitutions by maintaining persistent equations and variables in every cell. For brine and steam systems with high enthalpy, we adopt this formulation, using enthalpy as the state variable instead of temperature. The model is introduced in a novel fractional flow form, which enhances numerical efficiency. Fractures are modeled as two-dimensional objects within the surrounding three-dimensional porous medium, offering a mixed-dimensional extension of the multiphase flow model. This allows robust simulation of fluid flow, heat transfer, and phase separation, including the interaction between fractures and the porous medium. Our work makes two key contributions. First, we extend a compositional model to its mixed-dimensional version, enabling numerical simulations of fractured media in complex fracture networks. Second, we introduce an efficient interpolation scheme for H2O-NaCl brine in pressure-enthalpy-composition (PHZ) space, ensuring accurate representation of complex thermodynamic properties. We demonstrate the model's capabilities through simulations of geothermal flow in challenging fracture network geometries.

1. INTRODUCTION

Geothermal energy extraction requires a comprehensive understanding of the geological, physical, and geochemical properties of the reservoir, as well as the fluid properties of the geothermal fluids. To optimize energy extraction and improve reservoir management, robust and efficient numerical thermal simulation tools are essential (Zhu & Okuno, 2014, 2016; Connolly et al., 2021). Traditionally, simulations of mass and heat transfer in porous media include temperature as an independent variable, along with a set of natural variables. However, this approach requires variable substitution procedures to handle phase transitions, which adds complexity to the implementation. In contrast, the overall composition formulation offers the advantage of well-defined equations and variables at each cell, eliminating the need for variable substitution procedures (Voskov & Tchelepi, 2012).

Fractured geothermal systems present additional challenges. The intricate behavior of fractured media, which includes natural fractures and faults, can significantly affect fluid flow and thermal transport in the reservoir. These fractures act as key pathways for heat and mass transfer, and their geometry and connectivity must be accurately represented to predict reservoir performance (Kissling & Massiot, 2023). Despite advancements in simulation techniques, there is still a significant need for models that can accurately represent complex fracture geometries. Many existing models, such as TOUGH2, use multi-continua approaches to simulate flow (Bedoya-Gonzalez et al., 2022, 2023). The representation of fractures in these models lacks the precision needed to fully account for the impact of fracture connectivity and heterogeneity (Kissling & Massiot, 2023). This gap highlights the need for mixed-dimensional computational models, which can better represent the interaction between fractures and the surrounding matrix and serve as a baseline for developing and comparing with multi-continua approaches or other upscaling techniques.

In this paper, we present a novel mixed-dimensional compositional flow model tailored for high-enthalpy geothermal reservoirs, based on the overall composition formulation. The model incorporates a balance of mass, momentum, and energy transport, along with constitutive laws and closure relationships for non-isothermal multiphase flow in fractured media. We explicitly represent fractures as lower-dimensional objects, allowing for a more accurate modeling of fracture-matrix interactions. The following sections outline the mathematical formulation, including the governing equations, initial and boundary conditions. We then present numerical results from simulations of high-enthalpy geothermal systems, demonstrating the impact of fracture connectivity, heat transfer, and miscible phase transitions. Finally, we offer some concluding remarks.

2. MATHEMATICAL MODEL

This section presents the mathematical model, including the geometry with an explicit representation of the fractures, the conservation equations, constitutive relationships, and closure expressions for all dimensional objects, along with the initial and boundary conditions. It concludes with the definition of the continuous problem to be solved.

The mathematical model can be seen as extension to compositional flow of the mixed-dimensional mathematical model for single-phase flow in fractured porous media presented by Martin et al. (2005). We propose a formulation that combines the compositional formulation provided by Faigle et al. (2015) with a fractional flow form of the equations (Chen, 2000).

This leads to an equivalent fractional flow formulation consistent with Vehling et al., (2020) and verified using cases from Weis et al., (2014). A detailed verification of the implementation of this mathematical model is provided by Oguntola et al. (2025).

2.1 Geometry

In this subsection, the geometry is described in 2D. The extension to 3D follows similar concepts and ideas and is therefore not presented here. To simplify the model's presentation, we assume that all fractures share the same geometrical properties. However, the simulation framework allows for a fully dedicated set of parameters for each fracture in the domain.

Figure 1a depicts a 2D schematic representation of the matrix, fractures, and fracture intersections in an equi-dimensional geometry. Assuming a large aspect ratio between fracture length and width, Figure 1b presents fractures and their intersections as lines and points, respectively, in a mixed-dimensional geometry. This dimensional reduction is reflected into the original PDE system by defining partial differential equations (PDEs) on lower-dimensional objects (Martin et al., 2005; Flemisch et al., 2018; Berre et al., 2021), as shown in the following subsections.

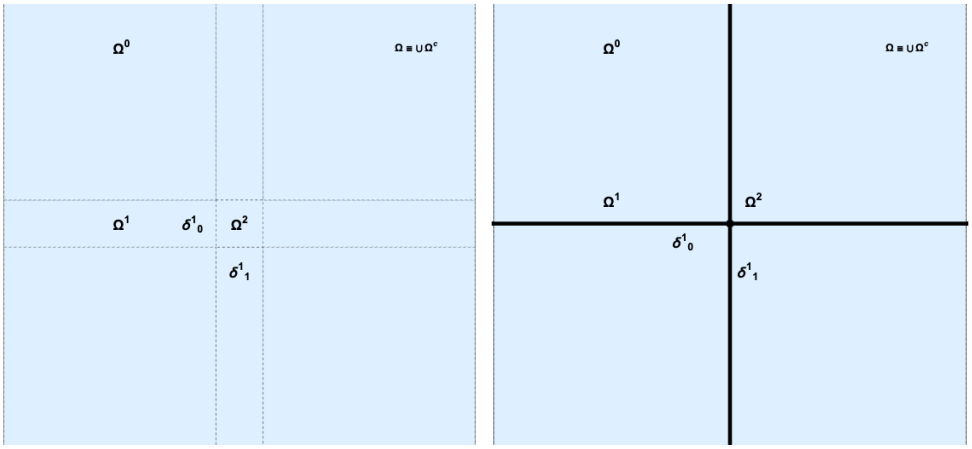

(a) (b)

Figure 1: Geometries: Schematic representations for the equi-dimensional domain (a) and the mixed-dimensional domain (b).

Let d_m denote the matrix dimension or the maximum dimension of the domain Ω and let d denote the subdomain dimension. Define the codimension as $c := d_m - d$. Let Ω^c denote the subdomain associated with c, such that $\Omega := \cup \Omega^c$. For instance, if $d_m = 2$, Ω^0 represents the rock matrix, Ω^1 represents the fractures and Ω^2 fracture intersections. This description is relevant to Figure 2, where a fracture Ω^c (red line) induces a pair of interfaces $\Gamma_{\pm}^c$ (grey lines) that connect the boundaries $\partial\Omega^{c-1}$ (blue lines).

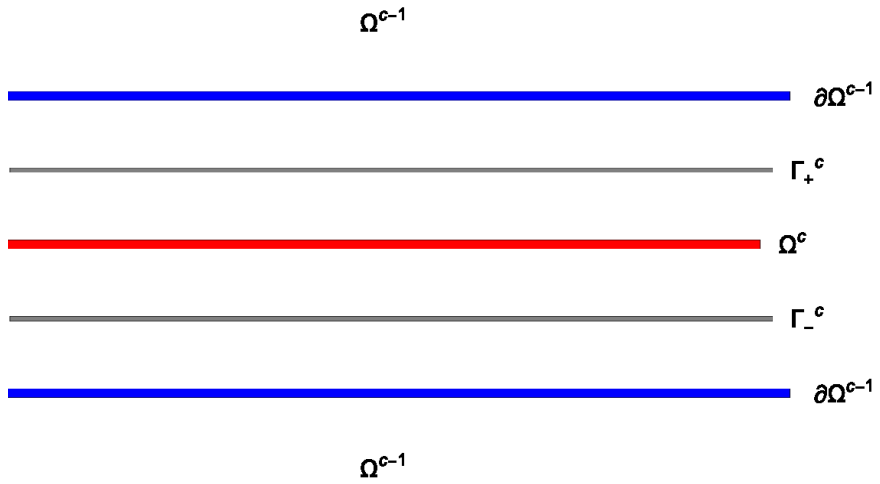

Figure 2: A fracture Ω^c (red line) inducing a pair of interfaces $\Gamma_{\pm}^c$ (grey lines) that connect the boundaries $\partial\Omega^{c-1}$ (blue lines). For illustration, the lines are shown separately in the figure, but in the mixed-dimensional domain, they geometrically coincide.

2.2 Mixed-dimensional conservation equations

Let define the jump as

$$(\cdot)_{\Gamma^c} = \begin{cases} \left(\cdot\,|_{\Gamma_+^c} + \cdot\,|_{\Gamma_-^c}\right) & for\ c > 0 \\ \emptyset & for\ c = 0 \end{cases}. \tag{1}$$

The mixed-dimensional conservation equations are as follows, starting with the overall mass balance:

$$\frac{\partial(\delta^c \phi \rho)}{\partial t} + \nabla \cdot \boldsymbol{m} + (m)|_{\Gamma^c} = 0,\ in\ \Omega^{\boldsymbol{c}}, \tag{2}$$

component mass balance:

$$\frac{\partial\left(\delta^c \phi \rho z_\xi\right)}{\partial t} + \nabla \cdot \left(\boldsymbol{m_\xi}\right) + \left(m_\xi\right)|_{\Gamma^c} = 0,\ in\ \Omega^{\boldsymbol{c}}, \tag{3}$$

overall energy balance:

$$\frac{\partial(\delta^c \phi(\rho h - p) + \delta^c(1-\phi)\rho_s c_s T)}{\partial t} + \nabla \cdot (\boldsymbol{q_a} + \boldsymbol{q_d}) + (q_a + q_d)|_{\Gamma^c} = 0,\ in\ \Omega^{\boldsymbol{c}}. \tag{4}$$

Note that the mathematical structure of the conservation Equations (2-4) consists of an accumulation term, a divergence operation, and the jump operator. The jump operator, as defined in Equation (1), connects the flux conserved between higher and lower-dimensional subdomains.

Table 2 presents the set of primary variables characterizing the state of the system of PDEs. If the mixture contains N_c components, the variables include pressure, $(N_c - 1)$-overall compositions, and the enthalpy equation.

Table 2: Set of primary variables.

Symbol	Physical field	Unit
p	Pressure	MPa
z_ξ	Overall component fraction	-
h	Specific enthalpy of fluid mixture	MJ/Kg

2.3 Mixed-dimensional constitutive equations

Since the balances above involve differential operators on vectorial fluxes, it is natural to provide the following constitutive relationships for each flux. In the following set of equations, δ^c represents the fracture width (in meter) raised to the power of the codimension c, such that for $c = 2$, $\delta^c \Longrightarrow \delta^2$ is given in square meters.

The gravity component in Darcy's law is given by

$$\boldsymbol{w}(\omega) = \lambda K\, \omega\, \boldsymbol{g},\ \ in\ \Omega^{\boldsymbol{c}}, \tag{5}$$

the overall mass flux is expressed as

$$\boldsymbol{m} = -\delta^c \lambda \boldsymbol{K} \nabla p + \delta^c \boldsymbol{w}(\boldsymbol{\rho}), in\ \Omega^{\boldsymbol{c}} \tag{6}$$

the component or phase mass flux is defined as

$$\boldsymbol{m_{\xi \vee \gamma}} = f_{\xi \vee \gamma} \boldsymbol{m} + \boldsymbol{b_{\xi \vee \gamma}}, in\ \Omega^{\boldsymbol{c}} \tag{7}$$

the component or phase buoyancy flux is given by

$$\boldsymbol{b_{\xi \vee \gamma}} = \delta^c \sum_{\boldsymbol{\xi \vee \gamma}} f_{\xi \vee \gamma} f_{\eta \vee \epsilon} \boldsymbol{w}\left(\rho_{\xi \vee \gamma} - \rho_{\eta \vee \epsilon}\right),\ in\ \Omega^{\boldsymbol{c}}, \tag{8}$$

the advective overall energy flux is expressed as

$$\boldsymbol{q_a} = \delta^c \sum_{\boldsymbol{\xi}} h_\gamma f_\gamma\, \boldsymbol{m},\ \ in\ \Omega^{\boldsymbol{c}}, \tag{9}$$

the diffusive overall energy flux is given by

$$\boldsymbol{q_d} = -\delta^c \boldsymbol{K_e} \nabla T \ \ in\ \Omega^c. \tag{10}$$

2.4 Mixed-dimensional coupling equations

The set of fluxes in Equations (5–10) is not arbitrary, as each flux has a corresponding counterpart defined on the interfaces $\Gamma_{\pm}^{c}$ acting in the direction perpendicular to the lower-dimensional subdomains. This establishes a set of coupling conditions between the partial differential equations (PDEs) defined on each subdomain.

The gravity component in Darcy's law is given by

$$w(\omega) = \lambda k_{\perp} \omega\, \boldsymbol{g} \cdot \boldsymbol{n},\ on\ \Gamma_{\pm}^{c}, \tag{11}$$

the overall mass flux is expressed as

$$m = -\lambda k_{\perp} \frac{2}{\delta^c} (p|_{\partial\Omega^{c-1}} - p|_{\Omega^c}) + w(\rho),\ on\ \Gamma_{\pm}^{c}, \tag{12}$$

the component or phase mass flux is defined as

$$m_{\xi \vee \gamma} = f_{\xi \vee \gamma} m + b_{\xi \vee \gamma},\ on\ \Gamma_{\pm}^{c} \tag{13}$$

the component or phase buoyancy flux is given by

$$b_{\xi \vee \gamma} = \sum_{\xi \vee \gamma} f_{\xi \vee \gamma} f_{\eta \vee \epsilon} w\left(\rho_{\xi \vee \gamma} - \rho_{\eta \vee \epsilon}\right),\ on\ \Gamma_{\pm}^{c}, \tag{14}$$

the advective overall energy flux is expressed as

$$q_a = \sum_{\xi} h_{\gamma} f_{\gamma}\, m,\ \ on\ \Gamma_{\pm}^{c}, \tag{15}$$

the diffusive overall energy flux is given by

$$q_d = -k_{e\perp} \frac{2}{\delta^c} (T|_{\partial\Omega^{c-1}} - T|_{\Omega^c}),\ on\ \Gamma_{\pm}^{c}. \tag{16}$$

2.5 Closure relationships

To complete the system of Equations (2–16), two groups of quantities must be defined. One group pertains to fluid mobility-related quantities, while the other describes fluid properties. The first group is detailed in Table 3, while the second is described in the following subsubsection.

Table 3: Definition of mobility-related quantities.

Quantity	Description
$\lambda_{\xi\gamma} \coloneqq \chi_{\xi\gamma} \rho_{\gamma} \frac{\kappa_{\gamma}}{\mu_{\gamma}}$	Mass-weighted mobility of component ξ in phase γ
$\lambda_{\xi} \coloneqq \sum_{\gamma} \lambda_{\xi\gamma}$	Mass-weighted mobility of component ξ
$\lambda_{\gamma} \coloneqq \sum_{\xi} \lambda_{\xi\gamma}$	Mass-weighted mobility of phase λ
$\lambda \coloneqq \sum_{\xi} \lambda_{\xi} \equiv \sum_{\gamma} \lambda_{\gamma}$	Total mass-weighted mobility
$f_{\xi} \coloneqq \frac{\lambda_{\xi}}{\lambda}$	Fractional flow of component ξ
$f_{\lambda} \coloneqq \frac{\lambda_{\lambda}}{\lambda}$	Fractional flow of phase λ

Table 2 presents mobility-related quantities that link the formulation in this document to the classical form of the multiphase multicomponent system (Faigle et al., 2015). Note that the subscripts $\xi - \eta$ and $\gamma - \epsilon$ are reserved for component and phases, respectively.

The partial fractions $\chi_{\xi\gamma}$ of component ξ in phase γ, along with the fractional flows f_ξ and f_γ, satisfy $\sum_\xi \chi_{\xi\gamma} = 1$, $\sum_\xi f_\xi = 1$ and $\sum_\gamma f_\gamma = 1$.

2.5.1 The system H2O-NaCl

The equilibrium problem of a compositional multiphase mixture is described by a set of nonlinear algebraic equations, known as the flash problem. Let denote $X = \{p, h, z_\xi\}$ the set of primary variables and $Y = \{T, \chi_{\xi,\gamma}, s_\gamma\}$ being the solution of the nonlinear algebraic equations for a given X. The flash problem can be represented as a mapping $\Phi: X \to Y$, which minimizes a scalar functional representing the Gibbs energy of the mixture (Gharbia et al., 2021).

For the specific case of the H_2O-NaCl system, it is possible to construct a set of correlations to represent the mapping Φ. These correlations are provided by Driesner & Christoph (2007), where both Y and the extra set $G = \{\rho_\gamma, h_\gamma, \mu_\gamma\}$ are expressed as functions of X, with G mapped by $\Phi_G: X \to G$.

Similar to Vehling et al. (2020), the mappings Φ and Φ_G are approximated using interpolated versions, $\widetilde{\Phi}$ and $\widetilde{\Phi}_G$. This is done in an offline stage, where the results are stored on disk as an interpolator object. During the numerical solution of the governing mixed-dimensional PDEs (online stage), these interpolators serve as an efficient proxy for the flash problem. Thus, the efficiency of the approximated flash is translated to a cost-effective implementation of these interpolators.

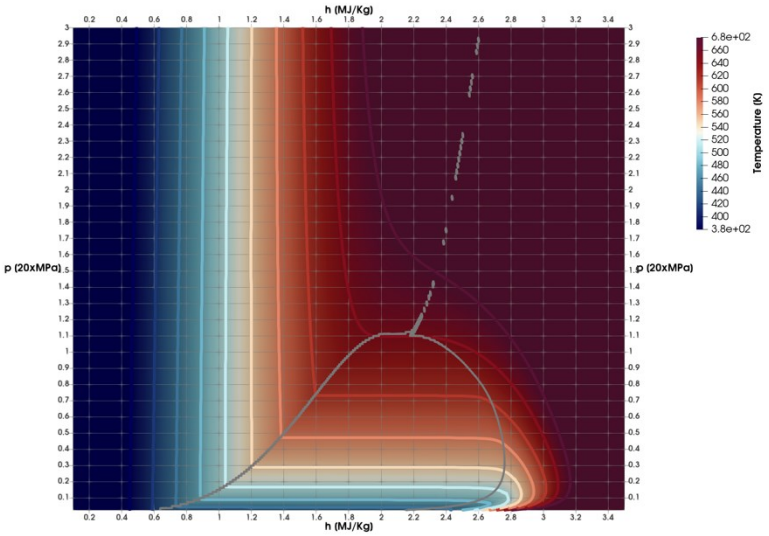

Figure 3: Pressure-enthalpy phase diagram for the H_2O-NaCl system at low $z_{NaCl} = 10^{-4}$.

Figure 3 presents a phase diagram in the parametric space $X = \{p, h, z_{NaCl} = 10^{-4}\}$. Driesner & Christoph (2007) provide a complete visualization and the topological structure of this phase diagram. A Cartesian VTK mesh is generated using regularly spaced samples of pressure, enthalpy, and NaCl overall composition. The quantities from the set $Y \cup G$ are evaluated at each grid point and stored as scalar fields in the VTK structure. The phase boundaries are shown as gray contours, with isotherms for temperatures lower and higher than the water critical point. The isotherms within the envelope highlight regions in the parametric space where pressure-temperature formulations require special treatment to compute h. For example, for a given temperature inside the envelope, multiple enthalpy values exist. In contrast, using pressure-enthalpy as the specification ensures a single, well-defined temperature inside the envelop, even near the critical point. This justifies our choice of primary variables for the energy equation, where temperature is a secondary variable and enthalpy is the primary variable in our mathematical model. The critical region can be identified near the intersection of the gray contour and the isothermal line with value $T \approx 646.7\ [K]$.

2.6 Initial and Boundary conditions

The initial conditions are set by projecting the initial $p(t=0)$, $h(t=0)$, and composition $z_\xi(t=0)$ to obtain the piecewise approximated $\tilde{p}(t=0)$, $\tilde{h}(t=0)$, and $\tilde{z}_\xi(t=0)$. If temperature is given instead of enthalpy, a bisection method is used to compute $\tilde{h}(t=0)$.

To describe the multiphysics boundary condition, we define three primary subsystems. the overall mass system (p-system), the component mass system (z-system), and the overall energy system (h-system). The p-system is parabolic, the z-system is hyperbolic, and the h-system entails an advection-diffusion equation. Each case is described below using Dirichlet (D), and Neumann (N) boundary conditions. The boundary conditions are independent, so the decomposition of the boundary $\partial\Omega^c$ is defined separately for each subsystem. Additionally, the conditions are given per codimension, meaning they apply to the boundaries $\partial\Omega^c$ of the subdomains.

2.6.1 Boundary conditions for p-system

Let consider the boundary decomposition $\partial\Omega^c = \partial\Omega_D^c \cup \partial\Omega_N^c$ and $\partial\Omega_D^c \cap \partial\Omega_N^c = \emptyset$ and $\partial\Omega_D^c \neq \emptyset$. The pressure and overall mass flux conditions are, respectively

$$p = p_D,\ on\ \partial\Omega_{\mathrm{D}}^c, \tag{17}$$

$$\boldsymbol{m} \cdot \boldsymbol{n} = m_N,\ on\ \partial\Omega_{\mathrm{N}}^c. \tag{18}$$

2.6.2 Boundary conditions for z-system

Let define the boundary decomposition $\partial\Omega^c = \partial\Omega_{in}^c \cup \partial\Omega_{out}^c$ and $\partial\Omega_{in}^c \cap \partial\Omega_{out}^c = \emptyset$ and $\partial\Omega_{in}^c \neq \emptyset$. The inlet flux of component ξ is

$$\boldsymbol{m_\xi} \cdot \boldsymbol{n} = m_\xi,\ on\ \partial\Omega_{\mathrm{in}}^c. \tag{19}$$

2.6.3 Boundary conditions for h-system

Let define the boundary decomposition $\partial\Omega^c = \partial\Omega_D^c \cup \partial\Omega_N^c$ and $\partial\Omega_D^c \cap \partial\Omega_N^c = \emptyset$ and $\partial\Omega_D^c \neq \emptyset$. The temperature and energy flux conditions are, respectively

$$T = T_D,\ on\ \partial\Omega_{\mathrm{D}}^c, \tag{20}$$

$$\boldsymbol{q} \cdot \boldsymbol{n} = q_N,\ on\ \partial\Omega_{\mathrm{N}}^c. \tag{21}$$

2.7 Full system of equations

The set of equations (2-16) defines a system of nonlinear, strongly coupled PDEs that govern mass and energy balance, along with initial and boundary conditions and the constitutive mapping $\widetilde{\Phi}_G$. Let us denote this system by the continuous operator $D\big(X(t), Y(t)\big)$ and the set of local algebraic equations representing the flash problem as $F\big(X(t), Y(t)\big) := Y(t) - \widetilde{\Phi}\big(X(t)\big)$. The continuous problem is to find $\{p, h, z_\xi\}\ \forall\ t \in [0, t_f]$ such that:

$$\begin{bmatrix} R_D \\ R_F \end{bmatrix} = \begin{bmatrix} D\big(X(t), Y(t)\big) \\ F\big(X(t), Y(t)\big) \end{bmatrix} = \begin{bmatrix} 0 \\ 0 \end{bmatrix}, \tag{22}$$

where R_D and R_F represent the residual equations associated with PDEs and the flash equations.

3. DISCRETIZATOIN

This section briefly outlines the discretization approach in a concise manner. The main components of the scheme include the Finite Volume Multi-Point Flux Approximation (MPFA) for space, the Backward Euler method for time, first-order upwinding for viscous terms, and hybrid upwinding for buoyancy terms (Hamon & Tchelepi, 2016).

Let denote the discrete unknowns $\tilde{X} = \{\tilde{p}, \tilde{h}, \tilde{z}_\xi\}$, and $(t^n)_{0 \le n \le N}$ the discrete time nodes with $t^0 := 0$ and $t^N = t_f$. The discrete set of residual equations $\tilde{R}_D\left(\tilde{X}(t^n), \tilde{Y}(t^n)\right) = 0$ and $\tilde{R}_F\left(\tilde{X}(t^n), \tilde{Y}(t^n)\right) = 0$. The global discrete problem is to find $\{\tilde{p}(t^n), \tilde{h}(t^n), \tilde{z}_\xi(t^n)\}\ \forall\ n \in \{1, \dots, N\}$ such that

$$\begin{bmatrix} \tilde{R}_F\left(\tilde{X}(t^n), \tilde{Y}(t^n)\right) \\ \tilde{R}_F\left(\tilde{X}(t^n), \tilde{Y}(t^n)\right) \end{bmatrix} = \begin{bmatrix} 0 \\ 0 \end{bmatrix}, \tag{23}$$

the evaluation of $\tilde{R}_F\left(\tilde{X}(t^n), \tilde{Y}(t^n)\right)$ can be easily parallelized. For a particular time, node t^n, the Jacobian matrix $J\big(\tilde{X}(t^n), \tilde{Y}(t^n)\big)$ takes the algebraic form

$$J = \begin{bmatrix} \tilde{A} & \tilde{B} \\ \tilde{C} & \tilde{E} \end{bmatrix}. \tag{24}$$

Furthermore, the Schur complement technique is used to reduce the global problem to $\tilde{X}(t^n)$ only, resulting in the reduced Jacobian $J_r = \tilde{A} - \tilde{B}\tilde{E}^{-1}\tilde{C}$. Since we use the overall composition formulation with enthalpy as a variable, the structure of $\tilde{E}$ is block diagonal, making its inverse computationally inexpensive. The numerical tolerance for global Newton iterations is set to1e-8.

4. NUMERICAL RESULTS

The numerical examples simulate narrow-boiling behavior and residual trapping, along with the complex properties of geothermal fluids in the H2O-NaCl system. They include fractured domains, requiring a robust discretization framework to ensure accurate modeling and physical consistency in mixed-dimensional problems. The numerical scheme is implemented using the PorePy framework (Keilegavlen et al., 2021). Since the verification of the gravity component is still in progress, gravity is disabled in the simulations.

Regarding code verification, several simulation benchmarks for the co-dimension 0 case in 2D were established (Oguntola et al. 2025), ensuring the correctness of the numerical solution for non-fractured media. Building on this, we focus on more advanced scenarios, including fractured domains near the critical point with high enthalpies and two-phase miscible flow.

All properties are taken from Weis et al., (2014). In the results section, we present a series of advection-dominated examples, detailing the material properties and using the same correlations as Driesner & Christoph (2007). The relative permeabilities account for residual saturation in the liquid phase to demonstrate residual trapping in the boiling zone, where the liquid saturation settles at $s_l = 0.3$. This value is observed in the simulations and highlighted to emphasize the correctness of the implementation concerning the mathematical model.

4.1 Uni-directional flow

The initial conditions include a constant temperature and a linear pressure variation along a 2 [km] domain with a 10 [m] mesh resolution. After the initial time, 673.15 [K] high enthalpy steam enters the liquid region at 423.15 [K], triggering the system's dynamics. The time step size is set to 1 [year] and the final simulation time is set to $t_f = 2000$ [year]. To simulate a two-phase front during the steam's advancement, the pressure is kept below, but near, the critical point of pure H2O, with fixed boundary pressures of 18 [MPa] and 15 [MPa] (high-pressure case) and 13 [MPa] and 10 [MPa] (low-pressure case). These two cases result in narrow and wider two-phase flow fronts, respectively.

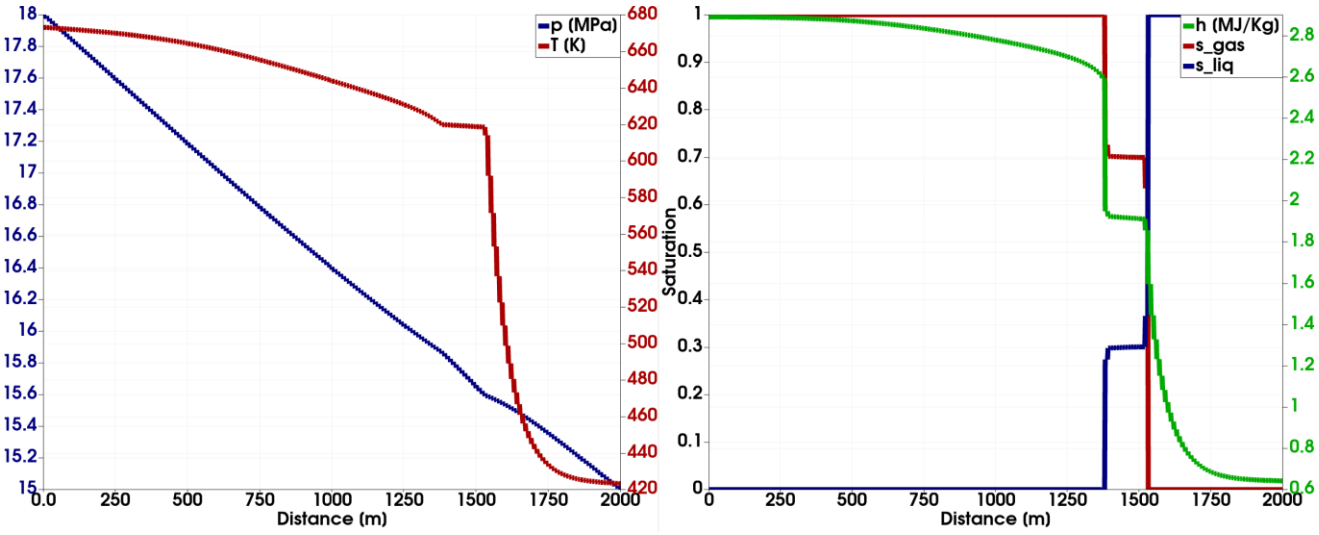

(a) (b)

Figure 4: High-pressure case: (a) Temperature and pressure profiles, and (b) Saturation and enthalpy profiles at 2000 years. The vertical axis colors correspond to the curve colors.

The two-phase region moves and transitions between high-enthalpy steam and low-enthalpy liquid zones, following the phase diagram shown in Figure 3. This can be easily understood by noting that in both cases, the pressure profile is nearly linear, or at least a slight perturbation from the initial linear profile (see the blue lines in Figures 4a and 5a), and the enthalpy ranges between 0.6 and 3 [MJ/kg]. In case 1, the system transitions between the points (18 [MPa], 3.0 [MJ/kg]) and (15 [MPa], 0.6 [MJ/kg]), and in case 2, between (15 [MPa], 3.0 [MJ/kg]) and (13 [MPa], 0.6 [MJ/kg]). If a line is drawn in the diagram in Figure 3 connecting the points (18 [MPa], 3.0 [MJ/kg]) and (15 [MPa], 0.6 [MJ/kg]), it intersects the top part of the two-phase envelope (see the gray line in Figure 3), resulting in a narrow boiling zone, as shown in Figure 4b, where the transition between liquid and steam is approximately 125 [meter]. Now, if we draw another line connecting (15 [MPa], 3.0 [MJ/kg]) and (13 [MPa], 0.6 [MJ/kg]), this line represents a vertical shift of 5 [MPa] from the first line (case 1). This line intersects the lower part of the envelope, where the two-phase zone becomes wider, leading to a larger boiling zone of approximately 550 [meter], as seen in Figure 5b.

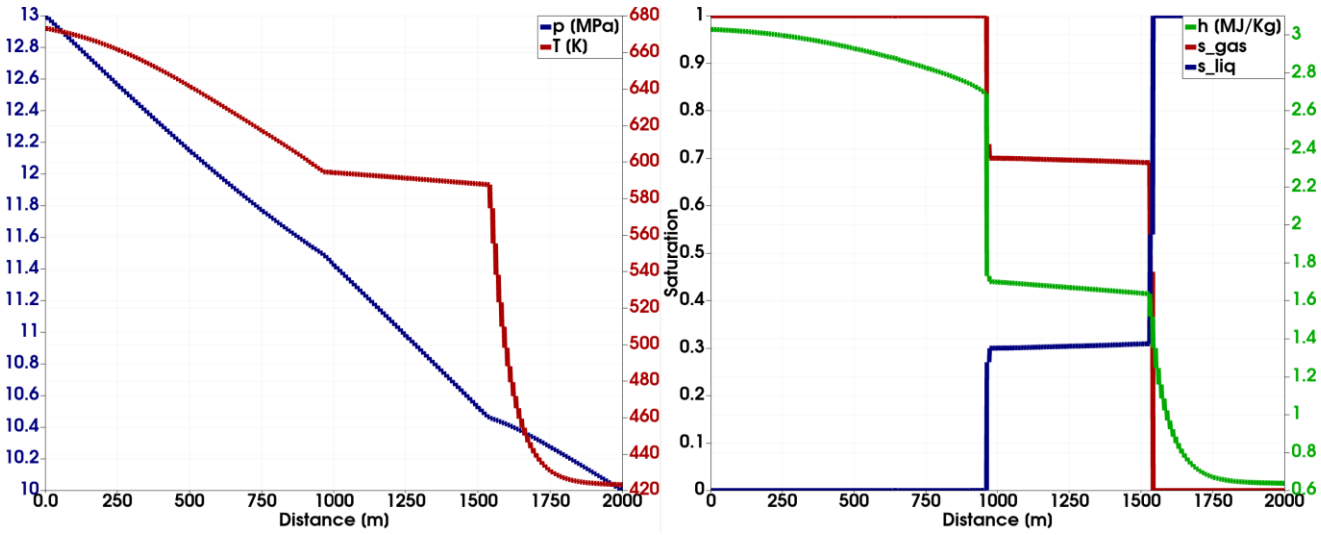

(a) (b)

Figure 5: Low-pressure case: (a) Temperature and pressure profiles, and (b) Saturation and enthalpy profiles at 2000 years. The vertical axis colors correspond to the curve colors.

Another important point to emphasize is that the situation depicted in Figure 4 shows a narrow boiling zone, which is naturally handled by the chosen set of primary variables and numerical scheme. Finally, the residual saturation of the liquid ($s_l = 0.3$) is observed in the two-phase zone. Interestingly, as the high-enthalpy steam move forward, it evaporates the trapped liquid, reducing the liquid saturation to zero.

4.2 Bi-directional flow in a fractured reservoir

The physical situation being modeled is a five-spot configuration in a horizontal region with faults. The domain for this study is based on the complex fracture network benchmark described in Section 4.3 of Flemisch et al. (2018). The geometry is scaled by a factor of 1000 [km]. The material parameters are the same as in the previous example. The key differences are constant initial pressure conditions: for case 1, the pressure is set to 15 [MPa], and for case 2, it is set to 10 [MPa]. The inlet pressure is 18 [MPa] for case 1 and 15 [MPa] for case 2. The injection is in the top-left corner, and production is in the bottom-right corner. The permeability for the fracture is 4 orders of magnitude larger than the matrix and the normal permeability $k_\perp$ is unitary, representing a highly conductive fault system. The time step size is set to 2 [year], with a final simulation time of $t_f = 1500$ [year]. Additionally, the system without faults is simulated to compare the changes in saturation fronts with and without fractures (see the gray lines in Figures 6b and 6d).

The configuration without faults shows a regular, symmetrical profile, demonstrating the expected behavior in 2D, as shown in Figures 6a and 6c. Since the grid resolution is not optimal, it is not clear to observe that the boiling zone is wider in the case with lower pressure conditions (Figure 6c). The residual liquid saturation ($s_l = 0.3$) is observed in the two-phase zone.

In the configuration with faults, the highly conductive fault system creates a larger, though less symmetrical, steam saturation front. Since we model fractures as lower-dimensional objects, boiling zones appear in all subdomains: matrix (plane), fractures (lines), and fracture intersections (points). Compared to the first case, the faulted configuration exhibits a larger boiling zone, as shown in Figure 6d. The residual liquid saturation ($s_l = 0.3$) is observed in the two-phase zone.

Figure 7 shows color maps for enthalpy in the top panels and temperature in the bottom panels. The left panels correspond to high pressure conditions, while the right panels correspond to low pressure conditions. Similar observations can be made here as in the uni-directional flow case. For enthalpy, we refer to the green curves in Figures 4b-5b, and for temperature, to the red curves in Figures 4a-5a.

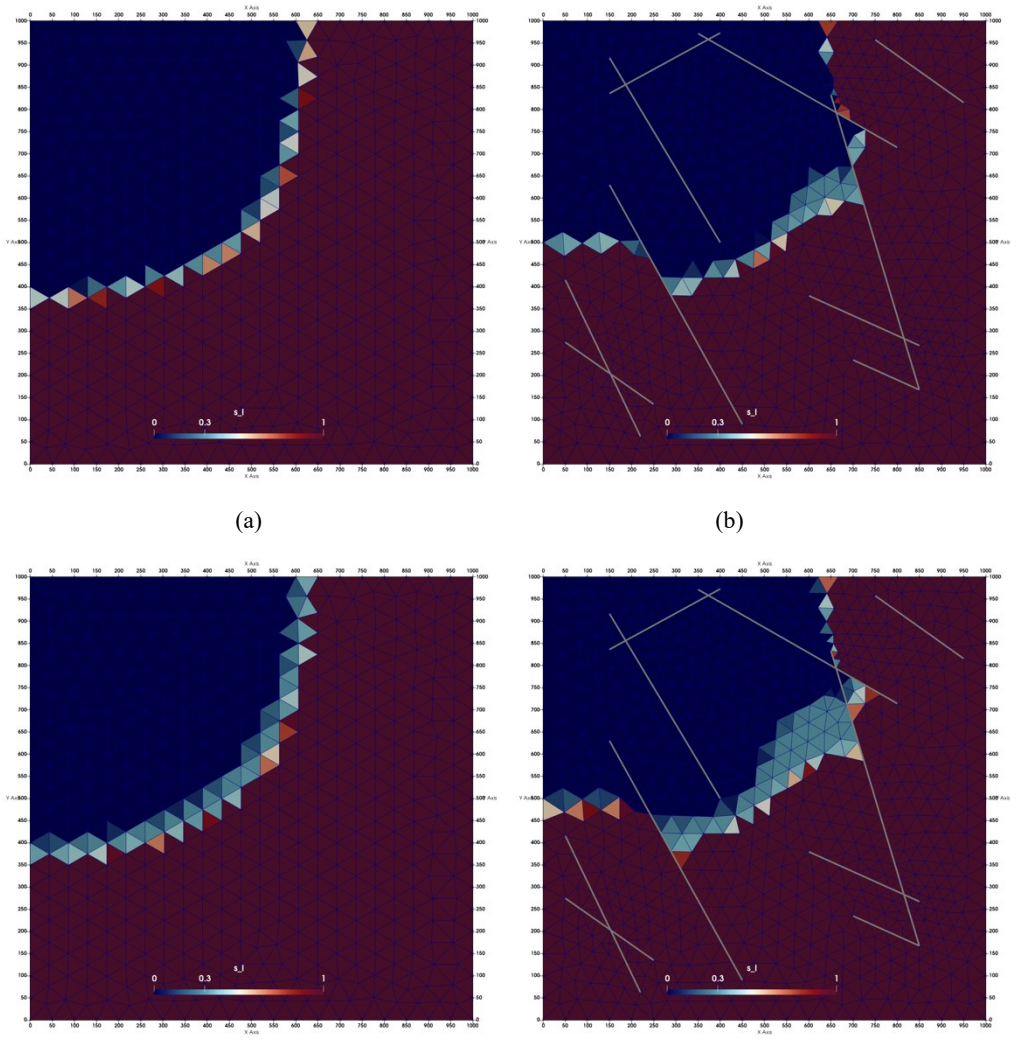

Figure 6: Liquid saturation profiles at 1500 [year]: (a) High pressure without faults, (b) High pressure with faults, (c) Low pressure without faults, and (d) Low pressure with faults. The gray lines represent the fault geometry.

For the high pressure conditions, the boiling zone enthalpy is approximately 2.0 [MJ/kg], as seen in Figure 7a (light-red color). In Figure 4b, enthalpy rapidly decreases from around 3.0 [MJ/kg] to a flat region of about 2.0 [MJ/kg], then smoothly drops to the initial value of 0.6 [MJ/kg]. A similar pattern is seen in the low pressure conditions, where the enthalpy decreases from 3.0 [MJ/kg] to a flat region of about 1.7 [MJ/kg] and then decreases smoothly to 0.6 [MJ/kg]. This is visible in Figure 7b (light-blue color).

For temperature, Figures 7c and 7d show similar trends: higher overall temperatures for high pressure conditions and lower overall temperatures for low pressure conditions. Additionally, due to the second-order Laplacian operator, the temperature color maps are more diffuse than the enthalpy color maps.

The simulations in this section show the implementation ability to handle fractured domains, high-enthalpy systems, and conditions near the critical point, all within a general compositional formulation tailored for geothermal systems. Additionally, including other correlations and fluid characterizations is straightforward by constructing the corresponding mapping $\widetilde{\Phi}$ and $\widetilde{\Phi}_G$.

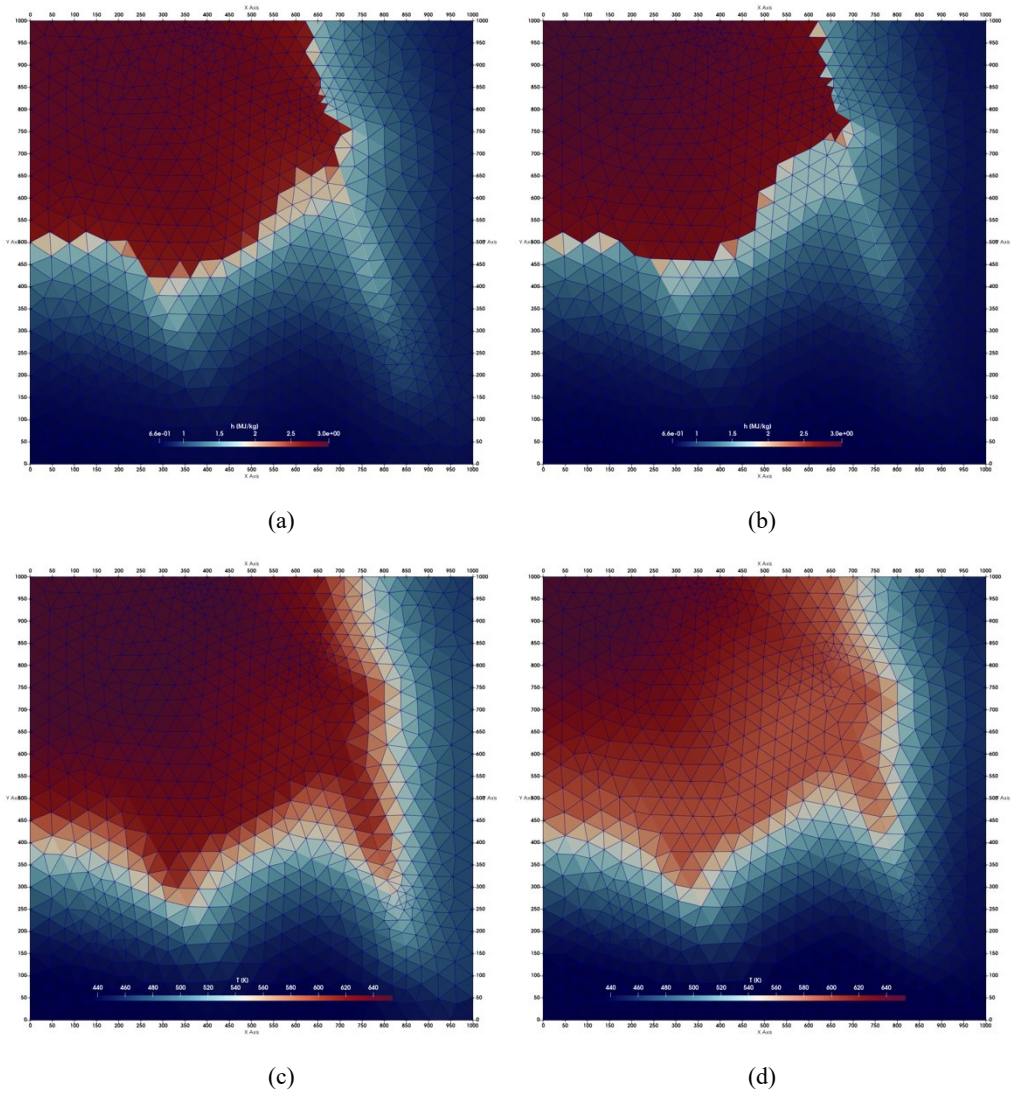

Figure 7: Thermal profiles at 1500 years: (a) Enthalpy for high pressure conditions, (b) Enthalpy for low pressure conditions, (c) Temperature for high pressure conditions, and (d) Temperature for low pressure conditions.

5. CONCLUSION

This paper introduces a novel mixed-dimensional compositional flow model for high-enthalpy geothermal reservoirs, based on the overall composition formulation. It bridges the advancements made in reservoir engineering for the simulation of green energy extraction, such as geothermal systems.

The formulation extends to modeling fractures as lower-dimensional objects, balancing compact notation with sufficient detail. The methodology incorporates complex constitutive expressions for the H2O-NaCl system, successfully verified to maintain physical consistency in mixed-dimensional problems. This consistency is demonstrated through examples with and without fractures.

Future work will further verify the gravity component and assess the convergence of the full mixed-dimensional computational model.

ACKNOWLEGMENT

This project has received funding from the European Research Council (ERC) under the European Union's Horizon 2020 research and innovation programme (grant agreement No 101002507).

REFERENCES

Bedoya-Gonzalez, D., Kessler, T., Rinder, T., Hilberg, S., Szabó-Krausz, Z., & Schafmeister, M.-T. (2023). A Multiple Interactive Continua Model (MINC) to Simulate Reactive Mass Transport in a Post-Mining Coal Zone: A Case Study of the Ibbenbüren Westfield. In Mine Water and the Environment (Vol. 42, Issue 2, pp. 266–292). Springer Science and Business Media LLC.

Bedoya-Gonzalez, D., Kessler, T., Rinder, T., & Schafmeister, M.-T. (2022). A dual-continuum model (TOUGH2) for characterizing flow and discharge in a mechanically disrupted sandstone overburden. In Hydrogeology Journal (Vol. 30, Issue 6, pp. 1717–1736). Springer Science and Business Media LLC.

Ben Gharbia, I., Haddou, M., Tran, Q. H., & Vu, D. T. S. (2021). An analysis of the unified formulation for the equilibrium problem of compositional multiphase mixtures. In ESAIM: Mathematical Modelling and Numerical Analysis (Vol. 55, Issue 6, pp. 2981–3016). EDP Sciences.

Berre, I., Boon, W. M., Flemisch, B., Fumagalli, A., Gläser, D., Keilegavlen, E., Scotti, A., Stefansson, I., Tatomir, A., Brenner, K., Burbulla, S., Devloo, P., Duran, O., Favino, M., Hennicker, J., Lee, I.-H., Lipnikov, K., Masson, R., Mosthaf, K., … Zulian, P. (2021). Verification benchmarks for single-phase flow in three-dimensional fractured porous media. In Advances in Water Resources (Vol. 147, p. 103759). Elsevier BV.

Chen, Z. (2000). Formulations and Numerical Methods of the Black Oil Model in Porous Media. In SIAM Journal on Numerical Analysis (Vol. 38, Issue 2, pp. 489–514). Society for Industrial & Applied Mathematics (SIAM).

Driesner, T., & Heinrich, C. A. (2007). The system H2O–NaCl. Part I: Correlation formulae for phase relations in temperature–pressure–composition space from 0 to 1000°C, 0 to 5000bar, and 0 to 1 XNaCl. In Geochimica et Cosmochimica Acta (Vol. 71, Issue 20, pp. 4880–4901). Elsevier BV.

Faigle, B., Elfeel, M. A., Helmig, R., Becker, B., Flemisch, B., & Geiger, S. (2015). Multi-physics modeling of non-isothermal compositional flow on adaptive grids. In Computer Methods in Applied Mechanics and Engineering (Vol. 292, pp. 16–34). Elsevier BV.

Flemisch, B., Berre, I., Boon, W., Fumagalli, A., Schwenck, N., Scotti, A., Stefansson, I., & Tatomir, A. (2018). Benchmarks for single-phase flow in fractured porous media. In Advances in Water Resources (Vol. 111, pp. 239–258). Elsevier BV.

Hamon, F. P., & Tchelepi, H. A. (2016). Analysis of Hybrid Upwinding for Fully-Implicit Simulation of Three-Phase Flow with Gravity. In SIAM Journal on Numerical Analysis (Vol. 54, Issue 3, pp. 1682–1712). Society for Industrial & Applied Mathematics (SIAM).

Keilegavlen, E., Berge, R., Fumagalli, A., Starnoni, M., Stefansson, I., Varela, J., & Berre, I. (2021). PorePy: an open-source software for simulation of multiphysics processes in fractured porous media. Computational Geosciences, 25, 243–265.

Kissling, W. M., & Massiot, C. (2023). Modelling of flow through naturally fractured geothermal reservoirs, Taupō Volcanic Zone, New Zealand. In Geothermal Energy (Vol. 11, Issue 1). Springer Science and Business Media LLC.

Martin, V., Jaffré, J., & Roberts, J. E. (2005). Modeling Fractures and Barriers as Interfaces for Flow in Porous Media. In SIAM Journal on Scientific Computing (Vol. 26, Issue 5, pp. 1667–1691). Society for Industrial & Applied Mathematics (SIAM).

Oguntola, M., Duran, O., Lipovac, V., Keilegavlen, E., & Berre, I (2025). A Unified Compositional Flow Model for Simulating Multiphase High-Enthalpy Geothermal Reservoirs. Proc, Fiftieth Workshop on Geothermal Reservoir Engineering Stanford University, Stanford, California.

Vehling, F., Hasenclever, J., & Rüpke, L. (2020). Brine Formation and Mobilization in Submarine Hydrothermal Systems: Insights from a Novel Multiphase Hydrothermal Flow Model in the System H2O–NaCl. In Transport in Porous Media (Vol. 136, Issue 1, pp. 65–102). Springer Science and Business Media LLC.

Voskov, D. V., & Tchelepi, H. A. (2012). Comparison of nonlinear formulations for two-phase multi-component EoS based simulation. In Journal of Petroleum Science and Engineering (Vols. 82–83, pp. 101–111). Elsevier BV.

Weis, P., Driesner, T., Coumou, D., & Geiger, S. (2014). Hydrothermal, multiphase convection of H2O-NaCl fluids from ambient to magmatic temperatures: a new numerical scheme and benchmarks for code comparison. In Geofluids (Vol. 14, Issue 3, pp. 347–371). Wiley.

Zhu, D., & Okuno, R. (2014). A robust algorithm for isenthalpic flash of narrow-boiling fluids. In Fluid Phase Equilibria (Vol. 379, pp. 26–51). Elsevier BV.

Zhu, D., & Okuno, R. (2016). Multiphase isenthalpic flash integrated with stability analysis. In Fluid Phase Equilibria (Vol. 423, pp. 203–219). Elsevier BV.